

Structure, magnetic and dielectric properties in nano-crystalline $\text{Yb}_2\text{CoMnO}_6$

Ilyas Noor Bhatti

Department of Physics, Jamia Millia Islamia University, New Delhi - 110025, India.

Imtiaz Noor Bhatti

Department of School Education, Government of Jammu and Kashmir, India.

Rabindra Nath Mahato

School of Physical Sciences, Jawaharlal Nehru University, New Delhi - 110067, India.

M. A. H. Ahsan

Department of Physics, Jamia Millia Islamia University, New Delhi - 110025, India.

Abstract

Structural, magnetic and dielectric properties have been studied for $\text{Yb}_2\text{CoMnO}_6$. Nano-crystalline sample of $\text{Yb}_2\text{CoMnO}_6$ synthesized by sol-gel method and structural analysis shows that the sample crystallizes in monoclinic crystal structure with $P2_1/n$ phase group. To understand the charge state of Co, Mn and Yb we have performed the XPS study. Magnetic study shows that the sample undergoes a paramagnetic to ferromagnetic phase transition around $T_c \sim 56$ K and an additional magnetic ordering at a lower temperature around 14 K due to ordering of Yb^{3+} magnetic ions. Temperature dependent Raman study reveals that spin-phonon interaction is present in this material. Further, we have studied the dielectric properties of this material. We observed that the material shows a relaxation behavior that obeys the thermally activated relaxation mechanism. Impedance spectroscopy reveals that the material shows non-Debye's behavior. AC conductivity study is performed to understand the conduction mechanics which involve the quantum mechanical tunneling phenomenon.

1. Introduction

Materials which simultaneously shows ferroelectricity and magnetism are termed as multiferroic materials.[1, 2] Strong coupling of electric and magnetic properties can be utilized for vast industrial applications, for instance, storage devices, sensors, tunable microwave filters, etc.[3, 4, 5, 6] Recently, several double perovskite materials have exhibited coupled magnetic and electric phenomenon. Among them, a new double perovskite $\text{Ba}_2\text{FeMnO}_6$ have shown co-existence of electric and magnetic hysteresis and considered as a promising candidate for spintronic applications.[7] The tunable magneto-electric effect has been observed in Y_2MnCrO_6 which have further intensified the quest of multiferroic materials in double

perovskites.[8] Interestingly, novel high-temperature multiferroicity have been observed in a $3d$ - $5d$ based $\text{Bi}_2(\text{Ni}/\text{Mn})\text{ReO}_6$ compound.[9] Despite having an interesting physics and exotic phenomenon with promising potential for industrial applications these materials have not been well studied.

Among the vast class of compounds $3d$ based R_2CoMnO_6 (where R = rare earth elements) has received much attention of researchers due to their exotic properties such as E type ferromagnetic ordering, spin-phonon coupling, multiferroicity, magnetoelectricity, etc. In these double perovskites the spin magnetic moment of Co^{2+} and Mn^{4+} interact via dominant super-exchange interaction and give rise to ferromagnetic ordering in these materials. However, in addition to this magnetic phase transition, the rare-earth ions also interact at low temperatures and in most cases align themselves in opposite direction to the Co/Mn

Email addresses: inoorbhatti@gmail.com (Ilyas Noor Bhatti), inbhatti07@gmail.com (Imtiaz Noor Bhatti)

sublattice and thus results in an antiferromagnetically ordered state. It is worth to mention some previous findings, for instance, $\text{Lu}_2\text{CoMnO}_6$ shows *E*-type magnetic ordering around 50 K with an anomaly in dielectric constant at same temperature which suggests some kind of magneto-electric interplay in this material.[10] Further, this material shows pyroelectric properties and has shown negative magnetocapacitance.[11] In another case, $\text{Er}_2\text{CoMnO}_6$ shows a ferromagnetic ordering of Co and Mn cations around 67 K with a low temperature ferrimagnetic ordering around 10 K activated by Er^{3+} ions.[12] The pyroelectric and polarization properties of Y_2CoMnO_6 have been studied and confirms that no intrinsic magnetoelectric multiferroicity exists.[13] Magnetization and neutron study of single crystalline $\text{Yb}_2\text{CoMnO}_6$ shows *E*-type ferromagnetic ordering and also shows negative magnetocapacitance.[10] Strong magnetic anisotropy and metamagnetic transition have been observed in a self flux-grown single crystal of $\text{Yb}_2\text{CoMnO}_6$. In this study, we aim to investigate the magnetic and dielectric properties of nano-crystalline $\text{Yb}_2\text{CoMnO}_6$ and compare the results with bulk study to identify the effect of reduced dimensions.

In the present study, we report structural, magnetic, dielectric and transport properties of nano-crystalline $\text{Yb}_2\text{CoMnO}_6$. The structural analysis shows the sample is in single phase and adopts the monoclinic crystal structure with $P2_1/n$ space group. Magnetization study reveals that the $\text{Yb}_2\text{CoMnO}_6$ is a ferromagnetic material that undergoes PM-FM phase transition around $T_c \sim 56$ K. The material also shows antiferromagnetic ordering at low temperature. Raman study shows spin-phonon coupling is present in this material. Dielectric measurement shows a strong dispersion in dielectric constant and tangent loss shows a relaxation phenomenon. The impedance spectroscopy shows that $\text{Yb}_2\text{CoMnO}_6$ does not follow Debye's model. The Nyquist plot analysis shows non-Debye's behavior $\text{Yb}_2\text{CoMnO}_6$. AC conductivity shows strong frequency dependency at the higher frequency limit. The conductivity analysis shows that the conduction mechanism involves the quantum mechanical tunneling phenomenon.

2. Experimental details

Sol-gel method has been employed to synthesize the nano-crystalline $\text{Yb}_2\text{CoMnO}_6$. Starting ingredients with high purity (99.9%) from Alpha Aesar were used. First, we have prepared solutions of each compound in separate beakers. We have dissolved $\text{Mn}(\text{CH}_2\text{CO}_2)_4 \cdot 4\text{H}_2\text{O}$, $\text{Co}(\text{NO}_3)_2 \cdot 6\text{H}_2\text{O}$ and nitric acid in water with continuous stirring till the solution becomes

clear. However, Yb_2O_3 is insoluble in water to make a clear solution we have added nitric acid drop by drop to the beaker containing Yb_2O_3 and water with continuous stirring at 95 °C. After continuous stirring for 20 minutes Yb_2O_3 dissolves completely in dilute nitric acid and the solution becomes clear. Then all the solutions were poured into the 500 ml beaker and filled to 400 ml with distilled water. This final solution is then kept on magnetic stirrer at 90 °C for 24 hours for suitable reaction time. The solution then turned into a gel and finally heated up to form a foam. The foam is collected from the beaker grounded well and heated at 600 °C. The collected powder is then grounded again for 30 minutes and sintered at 900 °C for 12 hours. The obtained powder is collected and characterized by X-ray diffraction using Rigaku mini flex 600 diffractometer. X-ray photoelectron spectroscopy (XPS) is performed to understand the charge state of cations. The XPS measurements were performed with base pressure in the range of 10^{-10} mbar using a commercial electron energy analyzer (Omicron nanotechnology) and a non-monochromatic $\text{Al}_{K\alpha}$ X-ray source ($h\nu = 1486.6$ eV). The XPSpeakfit software has been used to analyze the XPS data. The samples used for XPS study are in pellet form where an ion beam sputtering has been done on the samples to expose clean surface before measurements. The magnetic measurements were done on powder using a vibrating sample magnetometer by Cryogen.Inc. Temperature dependent Raman spectra have been collected using Diode based laser ($\lambda = 473$ nm) coupled with a Labram-HR800 micro-Raman spectrometer. It is a single spectrometer with 1800 grooves/mm grating and a peltier cooled CCD detector with an overall spectral resolution of ~ 1 cm^{-1} . For the low temperature Raman measurements, the material has been mounted on a THMS600 stage from Linkam UK, with temperature stability of ± 0.1 K. Dielectric measurements in the frequency range from 1 Hz to 5.5 MHz were performed using a computer controlled dielectric set up on a closed-cycle refrigerator with operating temperature range of 20 to 300 K.

3. Result and Discussions

3.1. Structural study

Fig. 1a shows the X-ray diffraction pattern along with Rietveld refinement for nano-crystalline $\text{Yb}_2\text{CoMnO}_6$ double perovskite. In this figure the black open circles are experimental data, the bold red solid line is the calculated model, the blue weak line is the difference in experimental and calculated pattern. The fitting parameter *goodness of fit* $\chi^2 = 1.93$ which is quite reasonable.

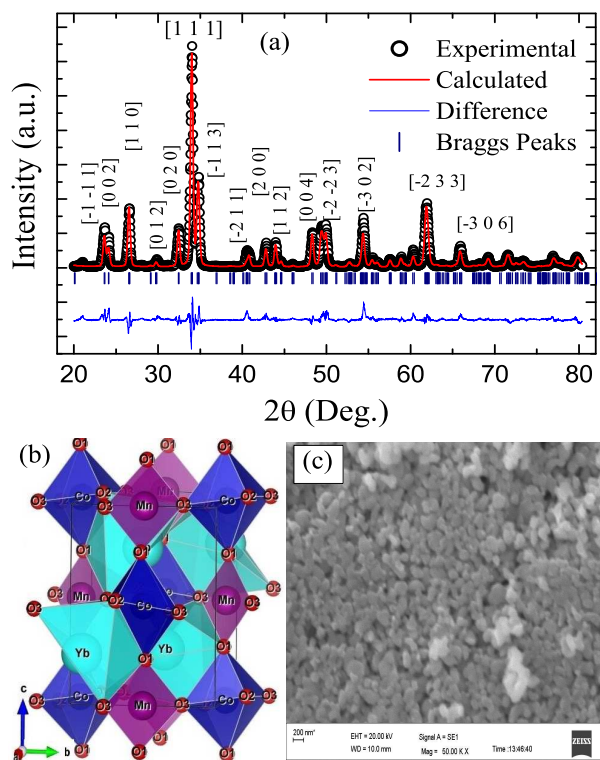


Figure 1: (Color online) (a) X-ray diffraction pattern along with Rietveld refinement for nano-crystalline $\text{Yb}_2\text{CoMnO}_6$, peak indexing is represented for main peaks. (b) Shows the monoclinic unit cell structure obtained from refinement data. (c) Representative SEM image use to estimate average particle size.

Further, from fitting we obtained R_{wp}/R_{exp} ratio ~ 1.38 which is reasonably good and acceptable.[14, 15, 16] These parameters show the Rietveld refinement is reasonably good. Bragg peaks are also shown with navy vertical bars. The Rietveld analysis on XRD data has shown that the sample is chemically pure and in single phase. Peak indexing is given in Fig. 1a for main peaks. The sample crystallized in monoclinic crystal structure with $P2_1/n$ space group. The lattice parameters are $a = 5.1535(8) \text{ \AA}$, $b = 5.5215(7) \text{ \AA}$, $c = 7.3832(5) \text{ \AA}$ and $\beta = 90.29(1)^\circ$ with the unit cell volume $210.08(9) \text{ \AA}^3$. The crystal structure unit cell is shown in Fig. 1b for this sample, it is evident from the figure that the Co and Mn atoms are alternatively placed. Further, to measure the average particle size we used the scanning electron microscope to obtain the micrograph of nano-particles as shown in Fig. 1c. The imageJ software is used to analyze the SEM micrograph and we found that the nano-particle of $\text{Yb}_2\text{CoMnO}_6$ are obtained with average particle size is $\sim 70 \text{ nm}$.

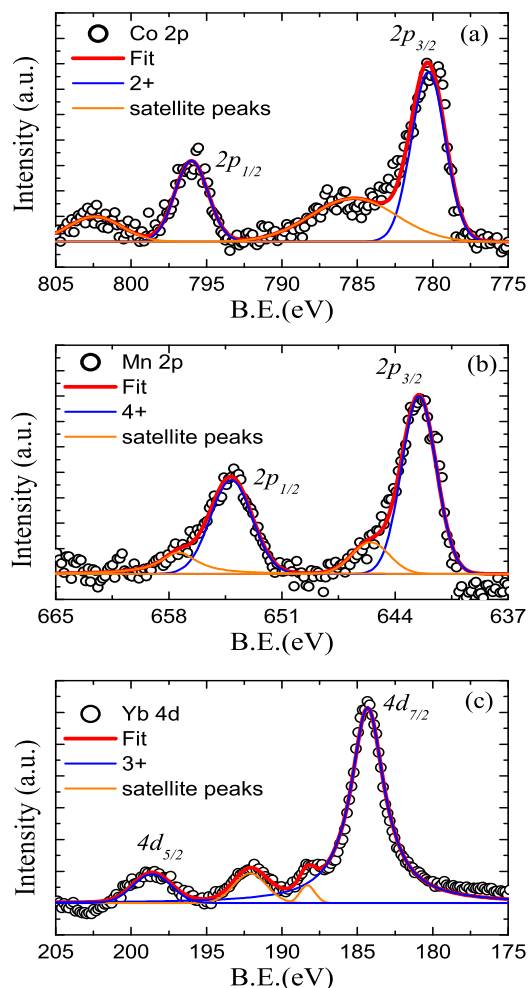


Figure 2: (Color online) (a) show the XPS core level spectra of Co 2p (b) show the XPS core level spectra of Mn 2p. (c) shows the XPS core level spectra of Yb 4d for $\text{Yb}_2\text{CoMnO}_6$. In the figure the red solid line is the overall envelope of the XPS spectrum and the other colored solid lines are the other respective fitted peaks.

3.2. X-ray photoelectron spectroscopy (XPS)

The physical properties of a compound are largely described by the oxidation state of cations present in the material. XPS is a vital tool to understand the charge state of cations. We have employed the XPS to study the cationic charge state of Co, Mn and Yb in $\text{Yb}_2\text{CoMnO}_6$. XPS spectrum of Co 2p is shown in Fig. 2a in which the open black circles are the experimental data the red line is the overall envelope of the spectrum the solid blue lines are the Co 2p peaks whereas orange solid lines are the satellite peaks fitted using XPS PEAKFIT 4.1. It is evident from Fig. 2a there are two peaks located at 780.7 eV and 796.01 eV for CO $2p_{3/2}$ and $2p_{1/2}$ respectively resulting from the spin-orbital split-

ting of $2p$ orbital with 15.3 eV. Besides the Co $2p$ there are two other peaks marked as satellite positioned at 787 eV and 802.5 eV. The results are consistent with literature.[17, 18, 19] Beside the Co $2p$ peaks two satellite peaks have also been observed close to Co $2p$ peaks. The peaks locations of Co $2p$ core level indicate that the Co cations are present in +2 oxidation states.

The measured XPS spectrum for Mn $2p$ core levels along with peak fitting is shown in Fig. 2b, where the open black circles are the experimental data the red line is the overall envelope of the spectrum the solid blue lines are the Mn $2p$ peaks are shown. The Mn $2p$ spectrum shows two distinct peaks located at 642 eV and 654 eV corresponding to Mn $2p_{3/2}$ and $2p_{1/2}$ resulting from the spin-orbital splitting of $2p$ orbitals with splitting energy of 12 eV. The peak positions and splitting energy is reveals that the Mn cation is present in +4 oxidation state and is in agreement with literature.[20, 21, 22]

XPS spectra of Yb $4d$ core level along with the fitting of peaks are shown in Fig. 2c where the open black circles are experimental data, the solid red line is the overall envelope of the XPS spectrum and solid blue lines are the Sm $3d$ orbitals. It is evident from the figure that the two distinct spin-orbital split peaks Yb- $4d_{5/2}$ and Yb- $4d_{3/2}$ peaks are located at 186 eV and 199.6 eV, respectively with at spin-orbital splitting energy of 13.6 eV. [23, 24] However, besides these two peaks there are more small peaks attributed to the presence of Yb $^{2+}$ oxidation state in the material. The detailed analysis of XPS spectrum reveals that the majority of Yb cations are present in +3 oxidation states whereas small Yb $^{2+}$ cations are also present.[24] It is conclusive from the XPS study that Co, Mn and Yb cations are in 2+, 4+ and 3+ oxidation states respectively.

3.3. Magnetization study

Temperature dependent magnetization ($M(T)$) measurements were performed both in the zero field cooled (ZFC) and field cooled (FC) mode as shown in Fig. 3a. ZFC and FC data is recorded in a temperature range of 300 K to 2 K under an applied dc magnetic field (H_{dc}) of 100 Oe. The figure shows that with the decrease in temperature the magnetic moment (M) in $M(T)$ curve remains steady initially. However, around 60 K the magnetic moment in both the (FC) and (ZFC) curve began to increase with a further decrease in temperature. It is expected that the rise in magnetic moment is due to establishment of magnetic exchange between Co^{2+} - Mn^{4+} in Yb_2CoMnO_6 double perovskite which is superexchange in nature and give rise to ferromagnetic ordering below 56 K. This sharp rise in the magnetic moment below 56 K is marked by paramagnetic (PM)

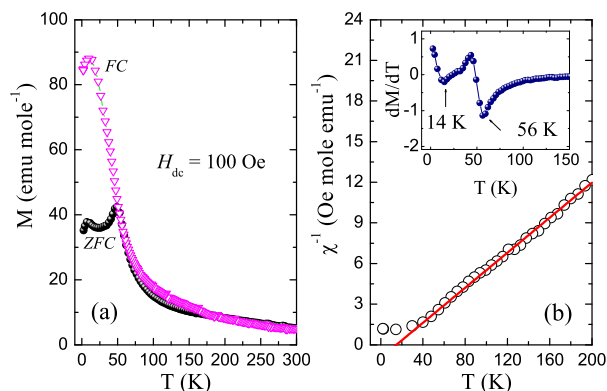


Figure 3: (Color online) (a) Temperature dependent magnetization data $M(T)$ shown for Yb_2CoMnO_6 measured at different fields. (b) $M(T)$ data plotted in terms of inverse susceptibility χ^{-1} , solid line is fitting due to Curie Weiss Law. Inset shows dM/dT vs T plot showing T_c for Yb_2CoMnO_6 .

to ferromagnetic (FM) phase transition in Yb_2CoMnO_6 . It is seen in Fig. 3a that the large bifurcation appears in M_{ZFC} and M_{FC} with further decreasing temperature. A peak like behavior around T_c is observed in M_{ZFC} curve and with further decreasing temperature the M_{ZFC} began to decrease, such type of behavior is seen in many perovskite compounds.[15, 16, 25, 26, 27, 28, 29] Whereas M_{FC} continuously increases with decreasing temperature. However, at low temperature below ~ 15 K there appears a peak in M_{FC} and M_{ZFC} which is related to the ordering of Yb^{3+} ions at low temperature. The bifurcation of ZFC and FC in oxides with composition $La_{0.7-x}Dy_xCa_{0.3}Mn(Fe)O_3$ has been studied in detail.[30, 31] The observation of such bifurcation is linked with the spin glass phase in this compound. However, the observed bifurcation is influenced by composition as reported and suppression of spin glass phase is observed. However, to better understand the bifurcation in ZFC and FC of Yb_2CoMnO_6 dynamic susceptibility measurement is required, where frequency dependent ac susceptibility can shed light on the presence of glassy phase in this material. To estimate the transition temperature across which magnetic phase transition from $PM - FM$ appears we have plotted the dM/dT vs T where the point of inflection in this plot gives the T_c . Inset Fig. 3b shows two points of inflection, one around 56 K the T_c corresponding to the ferromagnetic ordering of Co^{2+} - Mn^{4+} whereas the other appears at 14 K which is attributed to ordering of Yb^{3+} with net moment opposite to Co/Mn sublattice.

To further understand the magnetic behavior, we have plotted the temperature dependent magnetization data in terms of inverse magnetic susceptibility i.e. χ^{-1} vs T as

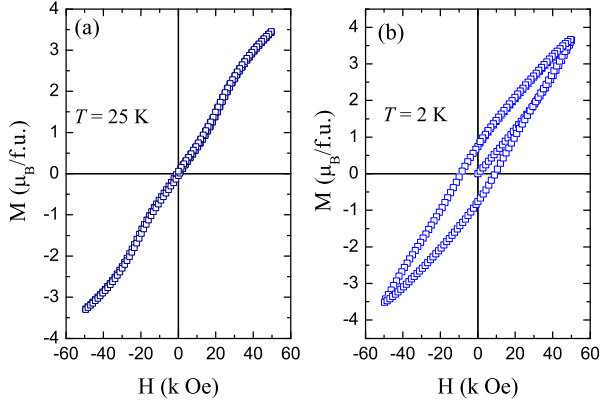


Figure 4: (Color online) Isothermal magnetization data collected at 25 K (see (a)) and 2 K (see (b)) in an applied magnetic field of up to ± 50 kOe for $\text{Yb}_2\text{CoMnO}_6$.

shown in the main panel of Fig. 3b. In the paramagnetic region above T_c , the inverse magnetic susceptibility can be fitted with conventional Curie Weiss law described as:[32, 33]

$$\chi = \frac{C}{T - \theta_p} \quad (1)$$

Here C is Curie Constant and θ_p paramagnetic Curie temperature. We have observed that the inverse susceptibility is varying linearly with the temperature above T_c . The susceptibility data of $\text{Yb}_2\text{CoMnO}_6$ in the temperature range 70 K to 200 K is fitted with Curie Weiss law given in Eq. 1. The fitting parameters obtained from fitting of χ^{-1} with Eq. 1 in Fig. 3b were used to calculate Curie constant and θ_p . The obtained values of C and θ_p for $\text{Yb}_2\text{CoMnO}_6$ are $15.470(2)$ emu K mole $^{-1}$ Oe $^{-1}$ and 14.08 K respectively. The positive value of θ_p signifies that the ferromagnetic ordering is present in $\text{Yb}_2\text{CoMnO}_6$ sample. Further, the effective magnetic moment is calculated using formula $\mu_{eff} = \sqrt{3Ck_B/N}$ where C is obtained from the slope of Curie Weiss fitting in Fig. 3b. The value of μ_{eff} is $11.12(6)$ $\mu_B/\text{f.u.}$

Isothermal magnetization i.e. the variation of magnetization against temperature $M(H)$ data have been collected at 25 K and 2 K up to ± 50 kOe applied magnetic field as shown in Fig. 4a and 4b respectively. $M(H)$ curve does not show any hysteresis at 25 K, however, we observe a slight slope change around 20 kOe in both positive and negative magnetic field directions. The $M(H)$ at 2 K is completely different from $M(H)$ curve at 25 K. $M(H)$ at 2 K shows a large hysteresis which suggests the overall ferromagnetic nature of $\text{Yb}_2\text{CoMnO}_6$. Further, the magnetic moment does not show any signs

of saturation even at the highest applied magnetic field of 50 kOe at both 2 K and 25 K. From the $M(H)$ curve at 2 K we found that the magnetic moment at 50 kOe is about 3.5 $\mu_B/\text{f.u.}$ whereas the remanent magnetization and coercive force are 0.8387 $\mu_B/\text{f.u.}$ and 9065 Oe respectively.

3.4. Temperature dependent Raman study

Temperature dependent Raman spectra taken at selective temperatures across magnetic transition is shown in Fig. 5a. The Raman spectra are taken in the temperature range from 10 K to 150 K across the magnetic transition whereas the Raman spectra are taken in the close temperature intervals across T_c . It is evident from Fig. 5a the important feature in the Raman spectra are the prominent Raman modes at 641 and 496 cm^{-1} corresponding to B_{2g} stretching mode and A_{1g} breathing mode respectively. These Raman modes are due to stretching, bending and rotation of (Co/Mn) O_6 octahedra. It is confirmed from the theoretical lattice dynamics that the strong sharp peak around 636 cm^{-1} originates from symmetric stretching of the (Co/Mn) O_6 octahedra, whereas the band at around 496 cm^{-1} describes a mixed type vibration of antisymmetric stretching and bending.[34] Additionally, the modes at ~ 1278 cm^{-1} represent the second-order overtones of the breathing mode.[35] The temperature dependent Raman spectra show variation in the peak positions and line width corresponding to each mode. The line shape along with the Lorentzian fitting is shown for phonon mode at 641 cm^{-1} is shown in Fig. 5b.

To understand the presence of spin-phonon coupling in $\text{Yb}_2\text{CoMnO}_6$, we have analyzed the Raman data of present series with the following anharmonic decay model:[26, 36]

$$\omega(T) = \omega_0 - C \left[1 + \frac{2}{\exp\left(\frac{\hbar\omega_0}{2k_B T}\right) - 1} \right] \quad (2)$$

where ω_0 and C are the intrinsic frequency of the optical mode and anharmonic coefficient, respectively. $\omega(T)$ describes the expected temperature dependence of a phonon mode frequency due to anharmonic phonon-phonon scattering.

The temperature dependent Raman shift ($\omega(T)$) at 641 cm^{-1} is shown in Fig. 6a. We have fitted the Raman mode with anharmonic decay model shown in Eq.2. The $\omega(T)$ fitted well with this model above T_c , however, we have observed that the $\omega(T)$ deviates

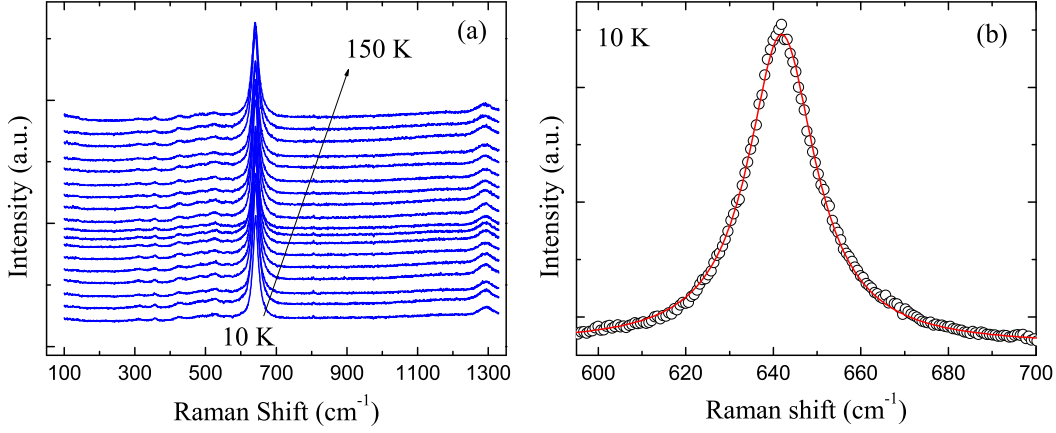


Figure 5: (Color online) (a) Raman spectra of $\text{Yb}_2\text{CoMnO}_6$ measured at different temperatures. (b) shows the line shape and its Lorentzian fitting of B_{2g} Raman mode at 641 cm^{-1} .

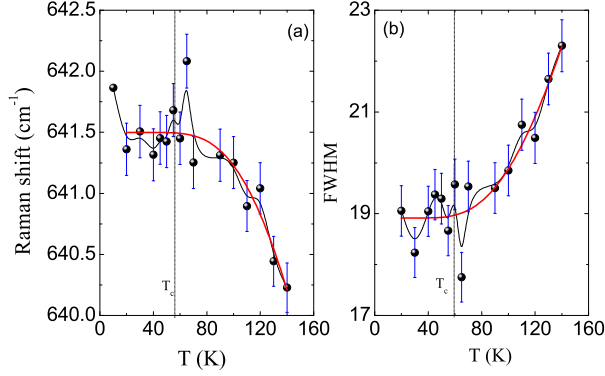


Figure 6: (Color online) Temperature Variation of (a) Raman shift (b) FWHM for Raman mode at 641 cm^{-1} corresponding to stretching of Co/MnO_6 for $\text{Yb}_2\text{CoMnO}_6$. The solid line is fitting due to Eq. 2

from anharmonic behavior around T_c shown in the figure where T_c guided by the dotted line. The deviation of $\omega(T)$ around T_c appears due to phonon renormalization caused by ferromagnetic ordering. This result suggests a spin-phonon coupling in $\text{Yb}_2\text{CoMnO}_6$. Such behavior has also been reported for many other compounds.[35, 36, 37] It is further noted that the temperature dependent line width of this phonon mode decreases with decreasing temperature as shown in Fig. 6b. It is evident from the figure that the line width also shows a deviation from anharmonic behavior across T_c . This deviation is attributed to the additional scattering mechanism involved such as spin-phonon coupling. Thus it is evident from Raman study that the spin-phonon coupling is present in $\text{Yb}_2\text{CoMnO}_6$.

3.5. Dielectric study

Fig. 7a and 7b represent the temperature dependent real and imaginary part of complex dielectric permittivity ϵ' and $\tan \delta$ respectively measured in the temperature range 20 K to 300 K at different frequencies for $\text{Yb}_2\text{CoMnO}_6$. Further, for relaxor systems with relaxation mechanisms, each relaxation component will correspond to plateaus in $\epsilon'(T)$ and respond with peaks in $\tan \delta$. For this material, we have observed that with increasing temperature the ϵ' at low temperatures ϵ' increases slowly however with increasing temperature ϵ' increases sharply. Further, with increasing frequencies, ϵ' decreases sharply. The higher value of ϵ' at low frequency is attributed to the accumulation of the charges at grain boundaries. On careful observation of tangent loss curve $\tan \delta$, it is seen that there is a broad hump at low temperature which is a feature of relaxor phenomenon. The observed relaxation is frequency dependent and shifts to higher temperatures with increasing frequency.

The relaxation mechanisms and its origin can be analyzed by fitting the peaks in $\tan \delta$ with the Arrhenius law given by, $\tau_{\tan \delta} = \tau_0 \exp(-E_a/K_B T)$ where, T is the temperature where peak occurs in tangent loss curve at a particular frequency $\tau_{\tan \delta}$, τ_0 and E_a are characteristic relaxation time and activation energy respectively and, k_B is the Boltzmann constant.[38, 39, 40, 42, 43]

Fig. 8 shows the variation of relaxation time with absolute temperature i.e. $\ln \tau$ vs $10^3/T$. It is evident from the figure that the relaxation time is well fitted with Arrhenius law which suggests the thermally activated relaxation mechanism. From the fitting parameters, we have calculated activation energy $E_a = 0.153 \text{ eV}$. To further understand the dielectric response we have mea-

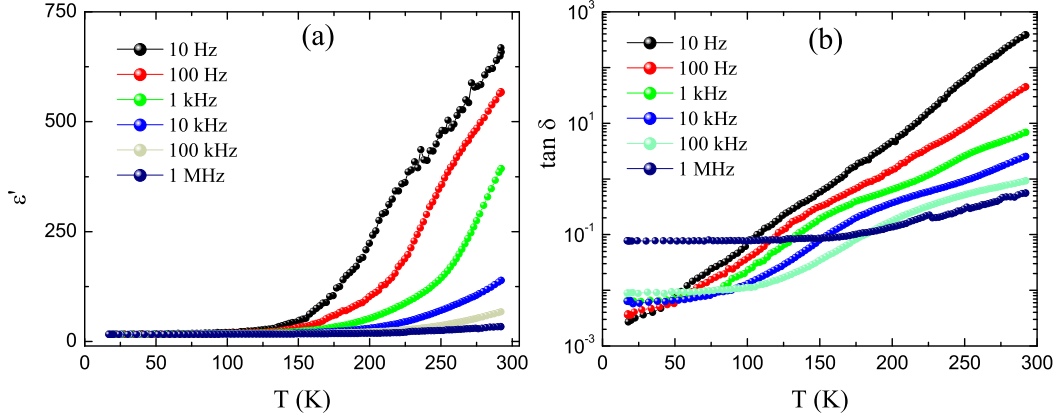


Figure 7: (Color online) Temperature dependent (a) real part of complex dielectric permittivity (ϵ') (b) loss tangent ($\tan \delta$) measure for $\text{Yb}_2\text{CoMnO}_6$ in the temperature range of 20 K to 300 K at various frequencies.

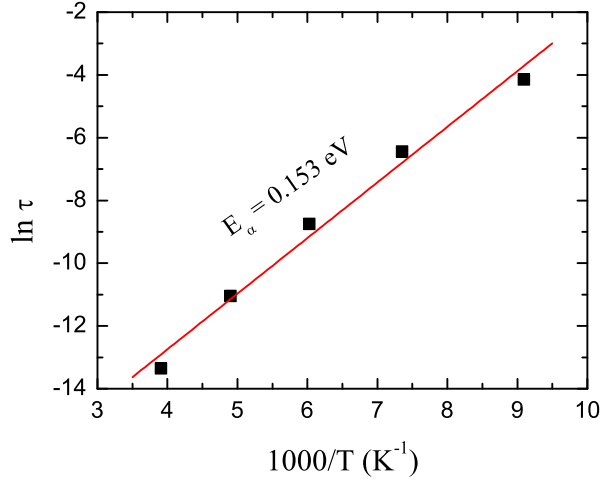


Figure 8: (Color online) Variation of relaxation time against normalized temperature i.e $\ln \tau$ vs $1000/T$ obtained from $\tan \delta$ plot.

sured the frequency dependent ϵ' and $\tan \delta$ over the frequency range 1 Hz to 5.5 MHz for $\text{Yb}_2\text{CoMnO}_6$ at different temperatures. In Fig. 9a we observed that $\text{Yb}_2\text{CoMnO}_6$ exhibits high dielectric constant at low frequency and high temperature. The dielectric spectrum is shown in Fig. 9a clearly shows two plateaus well separated by dispersion indicated by the arrow (Fig. 9a). The separate plateau in Fig. 9a are attributed to static and optical dielectric constant. Further, the frequency dependent dielectric constant shows the dispersion which moves to the higher frequency with increasing temperature. Fig. 9b shows the dielectric loss as a function of frequency measured at selective temperatures. The dielectric loss is relevant to the permittivity of the material.

3.6. Impedance spectroscopy

Fig. 10a shows the real part of complex impedance (Z') plotted as a function of frequency in the frequency range 1 Hz to 5.5 MHz at various temperatures between 50 K to 300 K. For clarity both the axis are in logarithmic scales. It is quite evident from the figure that the Z' decreases with increasing temperature. At low temperature Z' gradually decreases with increasing frequency, however, at the temperature above 100 K the Z' initially remains independent of frequency then at the higher frequency it began to decreases. Further, the frequency independent region moves to the high frequency region with increasing temperature. Further, it is observed that at high frequency and high temperature the Z' almost similar. This feature possibly is due to the release of accumulated space charges at high temperatures hence contribute to the enhancement of conduction in this material at high temperatures. The imaginary part of impedance (Z'') is shown in Fig. 10b for a wide frequency range. Z'' shows a peak which attains Z''_{max} for all the curves measured at different temperatures, further it is evident that the peak moves towards higher frequency with increasing temperature.

We know that the most probable relaxation time (τ) can be determined for relaxation system by identifying the position of the loss peak in the Z'' vs $\log(f)$ plots using the relation:[38, 39, 41, 42, 43]

$$\tau = \frac{1}{\omega} = \frac{1}{2\pi f} \quad (3)$$

where τ is relaxation time and f is the relaxation frequency. To further understand the relaxation behavior

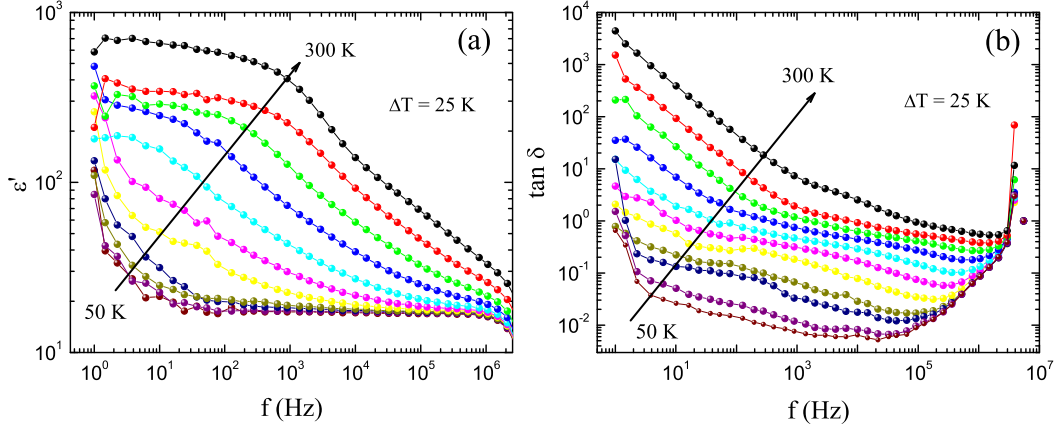


Figure 9: (Color online) Frequency dependent (a) real part of complex dielectric permittivity (ϵ') (b) loss tangent ($\tan \delta$) measure for $\text{Yb}_2\text{CoMnO}_6$ at various temperatures between 25 K and 300 K in the frequency range 1 Hz to 5.5 MHz.

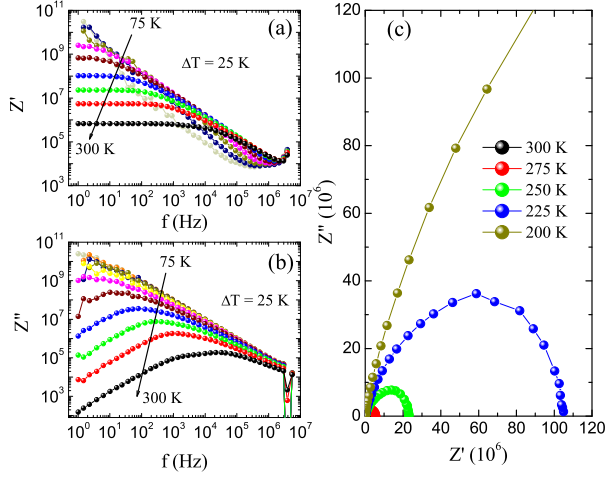


Figure 10: (Color online) (a) Frequency dependent real part of impedance Z' measure at different temperatures. (b) Frequency dependent imaginary part of impedance Z'' measure at various temperatures. (c) real Z' and imaginary part Z'' plotted in terms of Nyquist plot Z' vs Z'' .

we have plotted the relaxation time τ vs inverse temperature $10^3/T$ (K^{-1}). Fig. 11 shows the temperature variation of τ , it is observed that the relaxation time follows Arrhenius behavior given as: [42, 43, 44]

$$\tau_b = \tau_0 \exp\left(\frac{-E_a}{k_B T}\right) \quad (4)$$

where τ_0 is the pre-exponential factor, k_B the Boltzmann constant and T the absolute temperature. From the fitting parameters, the activation energy (E_a) has been calculated and is found to be 0.15 eV.

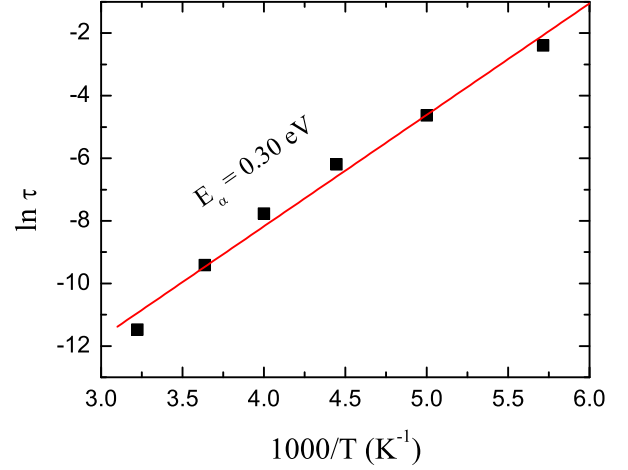


Figure 11: (Color online) Variation of relaxation time against normalized temperature i.e $\ln \tau$ vs $1000/T$ obtained from Z'' plot.

Fig. 10c shows the Z' vs Z'' in the form of Nyquist plots at some selective temperatures measure in the wide frequency range 1 Hz to 5.5 MHz. It is quite evident from the figures that the plot gives the semicircle in the whole range of temperature. The experimentally obtained impedance data for Yb_2CoMn_6 is plotted on the complex plane in terms of the Nyquist plot i.e. Z' vs Z'' . The semicircle in the Nyquist plots has depressed which suggests that the non-Debye type of relaxation is found in this material. It also manifests that there is a distribution of relaxation time instead of a single relaxation time in the material. Further, it is observed that the radius of semicircles decreases with increasing temperature.

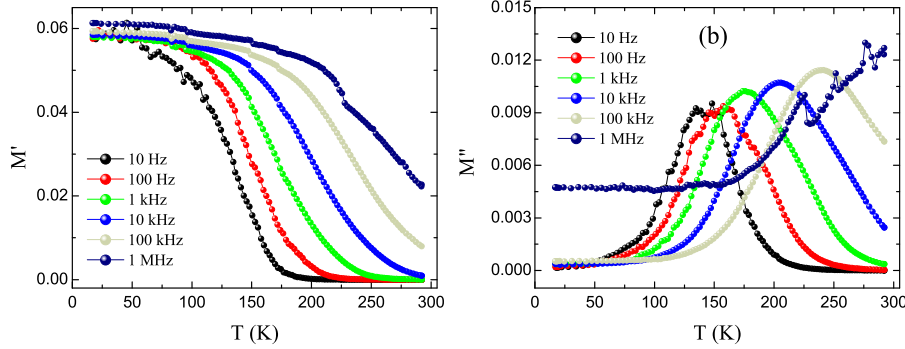


Figure 12: (Color online) (a) Variation of real part of electrical modulus (M') with temperature. (b) Imaginary part of electrical modulus M'' as a function of temperature.

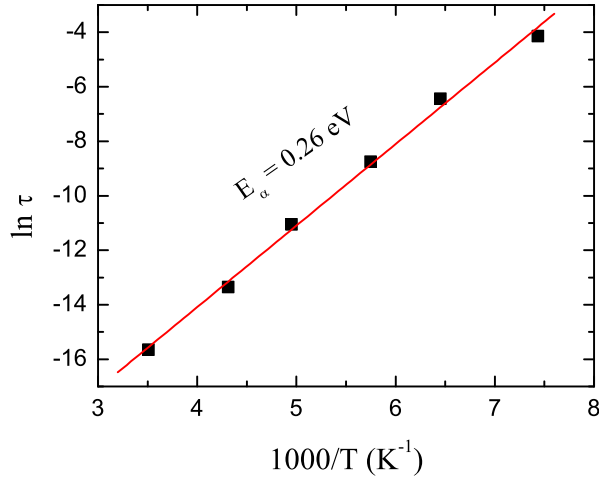


Figure 13: (Color online) Variation of relaxation time against normalized temperature i.e $\ln \tau$ vs $1000/T$ obtained from M' plot.

3.7. Electrical modulus

Information of interface polarization, relaxation time, electrical conductivity and grain boundary conduction effects, etc can be deduced from the electrical modulus of materials. Figs. 12a and 12b show the temperature dependent real (M') and imaginary (M'') part electrical modulus obtained at selective frequencies for Yb_2CoMnO_6 in the temperature range of 20 K to 300 K.

Fig. 12b shows variation of the M'' with frequency at selected temperatures. Once again, M'' spectroscopy plot reveals relaxation phenomena in the material. The maximum value (M'') in the M'' vs $\log f$ plot shows peak shifts to the higher frequency, which suggests that hopping of charge carriers is predominantly thermally activated. The asymmetric broadening of the peak indicates the spread of relaxation with different time con-

stants, which once again suggests the material is non-Debye-type.

To understand the relaxation mechanism we can have plotted the relaxation time as a function of absolute temperature i.e. τ vs $10^3/T$ shown in Fig. 13. The relaxation time is distributed and suggests that the relaxation mechanism is thermally activated in nature and follows Arrhenius behavior given by:[42, 43, 44]

$$\tau = \tau_0 \exp\left(\frac{-E_a}{k_B T}\right) \quad (5)$$

where τ_0 is pre-exponent factor, k_B is Boltzmann constant and E_a is the activation energy. we have fitted the data with above Eq. as shown in Fig. 13 and found that the data fitted well. From the fitting parameter we have calculated the activation energy $E_a = 0.26$ eV

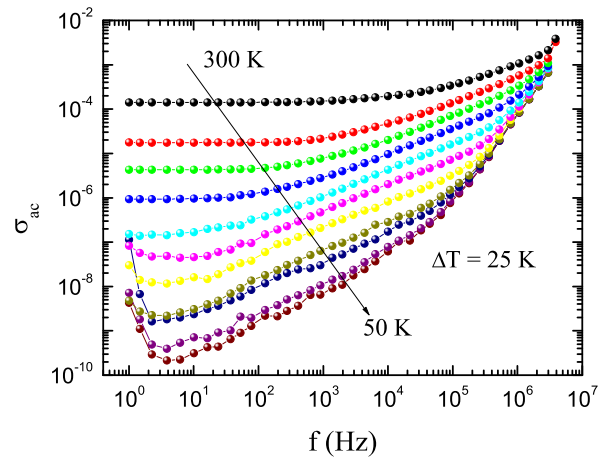


Figure 14: (Color online) Frequency dependence plot of the ac conductivity (σ_{ac}) for temperatures ranging from 50 K to 300 K are shown for Yb_2CoMnO_6 .

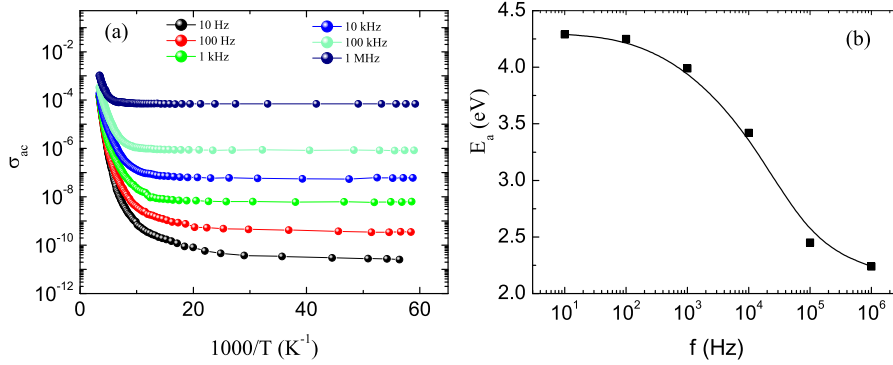


Figure 15: (Color online) (a) The variation of σ_{ac} with absolute temperature ($10^3/T$) is shown for Yb_2CoMnO_6 . The solid lines are due to fitting with Eqn. 7. (b) Variation of activation energy as a function of frequency for Yb_2CoMnO_6 .

3.8. Electric conductivity

To further understand the charge hopping and electrical properties we have investigated the AC conductivity in Yb_2CoMnO_6 . The AC conductivity is calculated by using the relation $\sigma_{ac} = \epsilon_0 \omega \epsilon''$. [45, 46] Fig. 14 shows the variation of AC conductivity with frequency i.e. σ_{ac} vs f at some selective temperatures in the range 50 K to 300 K. It is evident from the figure that at low frequencies the conductivity is independent of frequency and gives a plateau region at all temperatures. In this region of frequency, the conduction is mainly dominated by DC conductivity (σ_{dc}). However, at higher frequencies, the conductivity increases with increasing frequency. It is further to note that the plateau region marked by DC conductivity in Fig. 14 extends to the higher frequencies with increasing temperature. The frequency independent region also suggests that the hopping charges carrier are absent at low frequencies.

The variation of AC conductivity with absolute temperature i.e. σ_{ac} vs $10^3/T$ at some selective frequencies is shown in Fig. 15a. We observed that with increasing frequency the conductivity increases. To understand the conduction mechanism we have fitted the the conductivity with the following formula:[41, 47, 48]

$$\sigma_{ac} = \sigma_0 \exp\left(\frac{-E_a}{k_B T}\right) \quad (6)$$

where σ_0 is pre-exponent factor, k_B is Boltzmann constant and E_a is the activation energy. From the fitting parameters, we have calculated the activation energy. It is found that the activation energy E_a increases with decreasing frequency as shown in Fig. 15b.

4. Conclusion

Yb_2CoMnO_6 nano-crystalline was successfully synthesis by sol-gel method. In the present study, we report structural, magnetic, dielectric and transport properties of nano-crystalline Yb_2CoMnO_6 . The structural analysis shows that the sample is in single phase and adopt monoclinic crystal structure with $P2_1/n$ space group. Magnetization study reveals that the Yb_2CoMnO_6 is a ferromagnetic material that undergoes PM-FM phase transition around $T_c \sim 56$ K. The material also shows antiferromagnetic ordering at low temperature. Raman study shows spin-phonon coupling present in this material. Dielectric measurement shows a strong dispersion in dielectric constant and tangent loss shows a relaxation phenomenon. The impedance spectroscopy shows that Yb_2CoMnO_6 does not follow Debye's model. The Nyquist plot analysis shows non-Debye's behavior of Yb_2CoMnO_6 . AC conductivity shows strong frequency dependence at the higher frequency limit. The conductivity analysis shows that the conduction mechanism involves quantum mechanical tunneling phenomenon.

5. Acknowledgment

We acknowledge MNIT Jaipur, India for XPS data and AIRF (JNU) for magnetic measurement facilities. We acknowledge UGC-DAE-Consortium Indore and Dr. V. G. Sathe for Raman data. We also acknowledge Dr. A. K. Pramanik for dielectric measurement and UPEA-II funding for LCR meter. Author Ilyas Noor Bhatti acknowledges University Grants Commission, India for financial support.

References

- [1] K. F. Wang, J. M. Liu and Z. F. Ren, Adv. Phys. **58**, 321 (2009).

- [2] M. Fiebig, T. Lottermoser, D. Meier and M. Trassin, *Nat. Rev. Mater.* **1**(8), 16046 (2016).
- [3] J. T. Heron, M. Trassin, K. Ashraf, M. Gajek, Q. He, S. Y. Yang, D. E. Nikonov, Y-H. Chu, S. Salahuddin and R. Ramesh, *Phys. Rev. Lett.* **107**, 217202 (2011).
- [4] J. Seidel, L. W. Martin, Q. He, Q. Zhan, Y.-H. Chu, A. Rother, M. E. Hawkrigde, P. Maksymovych, P. Yu, M. Gajek, N. Balke, S. V. Kalinin, S. Gemming, F. Wang, G. Catalan, J. F. Scott, N. A. Spaldin, J. Orenstein and R. Ramesh, *Nat. Mater.* **8**, 229 (2009).
- [5] T. Hoffmann, P. Thielen, P. Becker, L. Bohat, and M. Fiebig, *Phys. Rev. B* **84**, 184404 (2011).
- [6] E. K. H. Salje, *Chem. Phys. Chem.* **11**(5) 940 (2010).
- [7] S. Ravi and C. Senthilkumar, *Ceramics International* **43**(16) 14441 (2017).
- [8] F. Yong, Y. Shi-Ming, Q. Wen, W. Wei, W. Dun-Hui and D. You-Wei, *Chin. Phys. B* **23**(11), 117501 (2014).
- [9] M. Lezai and N. A. Spaldin, *Phys. Rev. B* **83**, 024410 (2011).
- [10] J. Blasco, J. L. Garca-Muoz, J. Garca, J. Stankiewicz, G. Subas, C. Ritter and J. A. Rodriguez-Velamazn, *Appl. Phys. Lett.* **107**, 012902 (2015).
- [11] S. Yez-Vilar, E. D. Mun, V. S. Zapf, B. G. Ueland, J. S. Gardner, J. D. Thompson, J. Singleton, M. Snchez-Andjar, J. Mira, N. Biskup, M. A. Sears-Rodriguez and C. D. Batista, *Phys. Rev. B* **84**, 134427 (2011).
- [12] A. Banerjee, J. Sannigrahi, S. Giri, and S. Majumdar, *Phys. Rev. B* **98**, 104414 (2018).
- [13] J. Blasco, J. Garca, G. Subas, J. Stankiewicz, J. A. Rodriguez-Velamazn, C. Ritter, J. L. Garca-Munoz and F. Fauth, *Phys. Rev. B* **93**, 214401 (2016).
- [14] Ilyas Noor Bhatti, Imtiaz Noor Bhatti, R. N. Mahato and M. A. H. Ahsan, *Physics Letter A* **383**, 2326 (2019).
- [15] Imtiaz Noor Bhatti, R. S. Dhaka and A. K. Pramanik, *Phys. Rev. B* **96**, 144433 (2017).
- [16] Imtiaz Noor Bhatti, R. Rawat, A. Banerjee and A.K. Pramanik, *J. Phys.: Condens. Matter* **27**, 016005 (2014).
- [17] X. Wang, W. Li, X. Wang, J. Zhang, L. Sun, C. Gao, J. Shang, Y. Hu and Q. Zhu, *RSC Adv.* **7**, 50753 (2017).
- [18] B. Qiu, W. Guo, Z. Liang, W. Xia, S. Gao, Q. Wang, X. Yu, R. Zhao and R. Zou, *RSC Adv.* **7**, 13340 (2017).
- [19] H. Xia, D. Zhu, Z. Luo, Y. Yu, X. Shi, G. Yuan and J. Xie, *Scientific Reports* **3** 2978 (2013).
- [20] T. Hishida, K. Ohbayashi, and T. Saitoh, *J. Appl. Phys.* **113**, 043710 (2013).
- [21] R. C. Sahoo, D. Paladhi and T. K. Nath, *Journal of Magnetism and Magnetic Materials* **436**, 77 (2017).
- [22] Y. Cao, W. Li, K. Xu, Y. Zhang, T. Ji, R. Zou, J. Yang, Z. Qin and J. Hu, *J. Mater. Chem. A* **2**, 20723 (2014).
- [23] S. Ch. Sarma, U. Subbarao, Y. Khulbe, R. Jana and S. C. Peter, *J. Mater. Chem. A* **5**, 23369 (2017).
- [24] Z. Tiana, L. Zhengc, Z. Li, J. Li and J. Wanga, *Journal of the European Ceramic Society* **36**, 2813 (2016).
- [25] Ilyas Noor Bhatti, R. N. Mahato, Imtiaz Noor Bhatti, and M. A. H. Ahsan, *Physica B: Condensed Matter* **558**, 59 (2019).
- [26] Ilyas Noor Bhatti, Imtiaz Noor Bhatti, R. N. Mahato and M. A. H. Ahsan, *Ceramics International* **46**, 46 (2020).
- [27] Renu Gupta, Imtiaz Noor Bhatti and A. K. Pramanik, *J. Phys.: Condens. Matter* **32**, 035803 (2020).
- [28] Imtiaz Noor Bhatti and A. K. Pramanik, *Physics Letters A* **383**, 1806 (2019).
- [29] Ilyas Noor Bhatti, Rabindra Nath Mahato, Imtiaz Noor Bhatti and M.A.H. Ahsan, *Materials Today: Proceedings*, **17**, Part 1, 216 (2019).
- [30] S. C. Bhargava, S. Singh and S.K. Malik, *Journal of Magnetism and Magnetic Materials* **311**, 594 (2007).
- [31] S. C. Bhargava, S. Singh and S.K. Malik, *Phys. Rev. B* **71**, 104419 (2005).
- [32] S. Chikazumi, *Physics of ferromagnetism. English edition prepared with the assistance of C.D. Graham, Jr (2nd ed.)*. Oxford: Oxford University Press (2009)
- [33] B. D. Cullity and C. D. Graham, *Introduction to Magnetic Materials* John Wiley & Sons (2011)
- [34] M. N. Iliev, M. V. Abrashev, A. P. Litvinchuk, V. G. Hadjiev, H. Guo, and A. Gupta, *Phys. Rev. B* **75**, 104118 (2007).
- [35] C. Meyer, S. Hhn, M. Jungbauer, S. Merten, B. Damaschke, K. Samwer, and V. Moshnyaga, *J. Raman Spectrosc.* **48**, 46 (2017).
- [36] E. Granado, A. Garca, J. A. Sanjurjo, C. Rettori, I. Torriani, F. Prado, R. D. Sanchez, A. Caneiro and S. B. Oseroff, *Phys. Rev. B* **60**, 11879 (1999).
- [37] J. Laverdiere, S. Jandl, A. A. Mukhin, V. Yu. Ivanov, V. G. Ivanov, and M. N. Iliev, *Phys. Rev. B* **73**, 214301 (2006).
- [38] A. Schonhals and F. Kremer, *Broadband Dielectric Spectroscopy* Springer-Verlag Berlin Heidelberg (2003)
- [39] K. C. Kao, *Dielectric Phenomena in Solids: With Emphasis on Physical Concepts of Electronic Processes* Elsevier (2004).
- [40] Amantulla Mansuri, Ilyas Noor Bhatti, Imtiaz Noor Bhatti and Ashutosh Mishra, *Journal of Advanced Dielectrics* **08**, No. 04, 1850024 (2018).
- [41] J. E. Kim, S. J. Kim, H. W. Choi and Y. S. Yang, *J. Korean Phys. Soc.* **42**, 1224 (2003).
- [42] S. R. Elliott, *Adv. Phys.*, **36**, 135 (1987).
- [43] V. K. Bhatnagar and K. L. Bhatia, *J. Non-Cryst. Solids*, **119**, 212 (1990).
- [44] H. A. M. Ali and M. A. Ibrahim, *Materials Science-Poland*, **34**(2), 386 (2016).
- [45] A. Sing, A. Gupta and R. Chatterjee, *Appl. Phys. Lett.* **93**, 022902 (2008).
- [46] S. Thakur, R. Rai, Igor Bdikin and M.A. Valente, *Ceramics Mater. Res.* **19**, 1 (2016).
- [47] V. S. Puli, C. Orozco, R. Picchini and C. V. Ramana, *Materials Chemistry and Physics* **184**, 82 (2016).
- [48] C. Chen, P. Jost, H. Volker, M. Kaminski, M. Wirtsohn, U. Engelmann, K. Kruger, F. Schlich, C. Schlockermann, R. P. S. M. Lobo and M. Wuttig, *Phys. Rev. B* **95**, 094111 (2017).